



Optimization of FDM parameters for enhanced mechanical properties of chopped carbon fiber-reinforced polymer composites

Mohammad Rouhi Moghanlou¹ · Elaheh Azizian-Farsani¹ · Ali Mahmoudi¹ · Michael M. Khonsari¹

Received: 3 April 2024 / Accepted: 18 July 2024
© The Author(s), under exclusive licence to Springer Nature Switzerland AG 2024

Abstract

Properly selected values for fused deposition modeling (FDM) printing parameters can enhance the mechanical and microstructural characteristics of the 3-D printed part. For this purpose, the Taguchi method for the design of experiments (DOE) is employed in this study to determine optimal values for four FDM printing parameters when utilizing chopped carbon fiber-reinforced polyamide filaments. Optimization aims to maximize the ultimate tensile strength (UTS) and minimize inter-layer porosities, while also considering the printing time and the weight of the part. Tensile test specimens, designed according to the ASTM D638 standard, were printed using the parameter values determined by the Taguchi model. Additionally, cubic samples were printed using similar parameters, and their cross-sectional porosities were assessed through optical micrography and image processing software. The tensile test results exhibited significant variations in the UTS values of the specimens, ranging from 91.9 to 171 MPa, with porosities ranging between 1.4% and 17.63%. Based on the Taguchi model, an infill line distance of 0.4 mm, layer height of 0.3 mm, printing speed of 100 mm/s, and chamber temperature of 55 °C yielded in the most optimized specimen, as determined by the UTS/weight and UTS/time criterion. Subsequent tensile tests validated the prediction of the Taguchi optimization.

Keywords Additive manufacturing · 3D printing · FDM · Taguchi · Carbon fiber reinforced composites · Ultimate tensile strength

1 Introduction

Additive manufacturing (AM), through its layered construction approach, represents an important shift in manufacturing, surpassing traditional methods by offering exceptional design flexibility and precision in object fabrication. It offers unique efficiency in the production of diverse components across various industries while generating minimal waste compared to most traditional manufacturing techniques [1]. In particular, 3D printing via fused deposition modeling (FDM) is the most extensively employed AM method. The application of FDM is growing rapidly across diverse industries, including the automotive, aerospace, and medical sectors [2–4].

The most commonly used materials for the FDM printers include thermoplastics such as acrylonitrile butadiene

styrene (ABS) and polylactic acid (PLA) [5, 6], as well as more advanced thermoplastics such as polyethylene terephthalate (PET), polycarbonate (PC), and polyamide (PA) [7]. Carbon fiber-reinforced polymers (CFRPs) are produced by adding carbon fibers (CFs) to the plastic matrix material. This novel approach to AM technologies allows for the fabrication of complex geometries and structures that were previously unfeasible while still providing considerable strength-to-weight advantages similar to traditional CFRPs [8–11]. This integration significantly improves the mechanical properties of the final parts, including enhanced tensile strength, durability, and stiffness, making 3D-printed CFRPs ideal for aerospace and high-performance engineering applications [12, 13].

3D-printed CFRPs can be classified into two groups based on the CF type: short fibers and continuous fibers [14, 15]. The ability to control fiber orientation, volume fraction, and the infill pattern of the matrix in continuous fiber 3D-printed materials permits customization of the objects that meet specific usage requirements [16–18]. The combination of the strength and low weight of chopped

✉ Michael M. Khonsari
khonsari@lsu.edu

¹ Department of Mechanical and Industrial Engineering,
Louisiana State University, Baton Rouge, LA 70803, USA

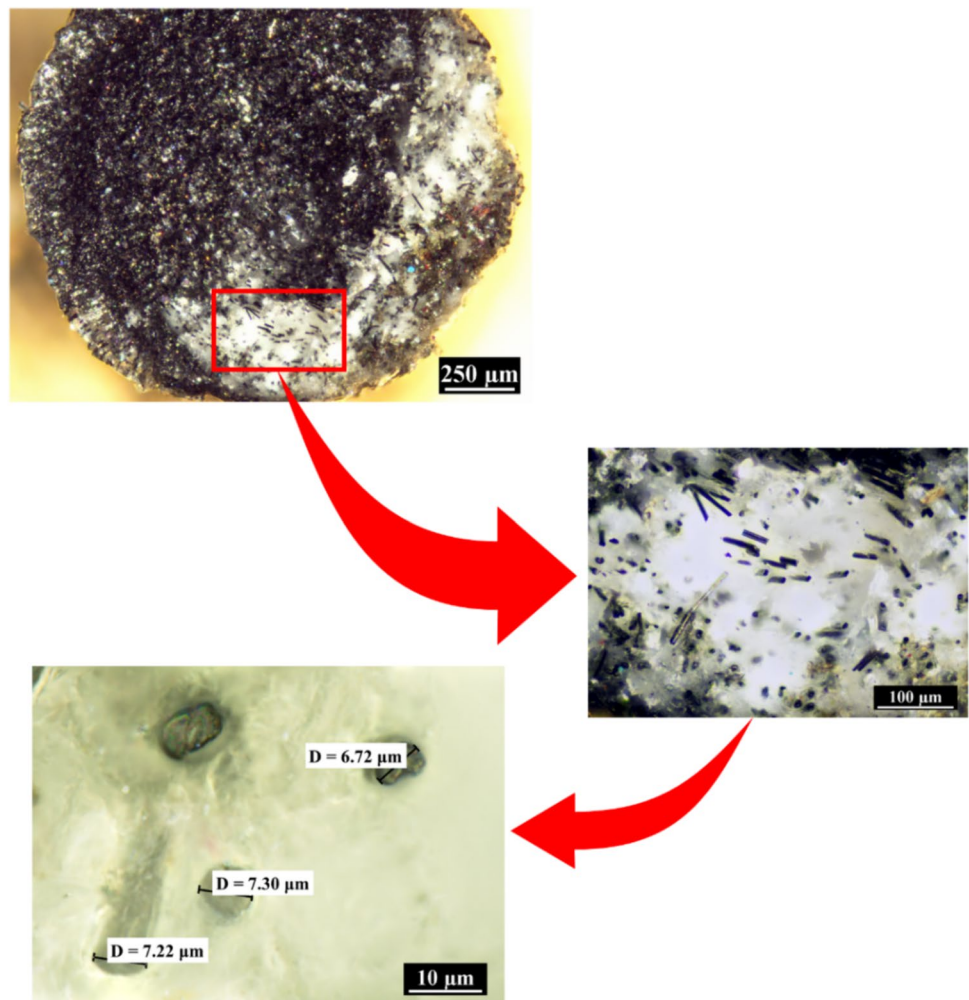
CFs with the adaptability of thermoplastic polymers offers a substantial advancement in the field of AM [19–21]. In contrast to unreinforced polymers, this technology enables the production of parts with mechanical properties that meet the design requirements of numerous engineering parts [22–24].

As noted, for applications requiring high strength-to-weight ratios, the isotropic reinforcement of the chopped fibers improves the final parts' performance and durability [6, 25]. To achieve higher fiber dispersion and more consistent material properties throughout printed components, advancements in material formulations are necessary for the printing process [26]. In a study by Almeshari et al., 3D-printed short CF-reinforced polypropylene (PP) composite filaments with varying carbon content (up to 22 wt.%) were developed [27]. The resulting short-CF/PP composites exhibited significant improvements in mechanical properties, a 150% increase in tensile strength, and a 260% enhancement in impact toughness. The study also highlighted microstructural characteristics, with the dominant failure mechanism identified as fiber pull-out during tensile loading.

Lobov et al. [28] showed that short CF-reinforced ABS has significantly improved mechanical properties compared to conventional ABS. This research also revealed a correlation between strength characteristics, elastic properties, and the diameter of the 3D printing nozzle. Thus, the possibility of increasing tensile strength, fracture toughness, and interlayer adhesion strength by adjusting the printing nozzle diameter was investigated [29]. In a separate study, researchers examined the mechanical properties of graphene blocks reinforced with chopped CF. The findings indicated that the inclusion of 0.8 wt.% CF led to a nearly 60% increase in flexural strength [30].

The application of Design of Experiments (DOE), particularly the Taguchi method has gained interest for optimizing 3D printing parameters [31–34]. Using a Taguchi experimental design and analysis of variance (ANOVA), Ahmed et al. optimized the FDM printing parameters for thermoplastic composites reinforced with oil palm fiber [35]. Their study investigated the effects of layer thickness, fiber orientation, infill density, and printing speed on the mechanical properties of printed specimens. They

Fig. 1 Microscopic images of the cross-section of CF-reinforced polymer filament. The length and diameter of the fibers are visible in the last two images



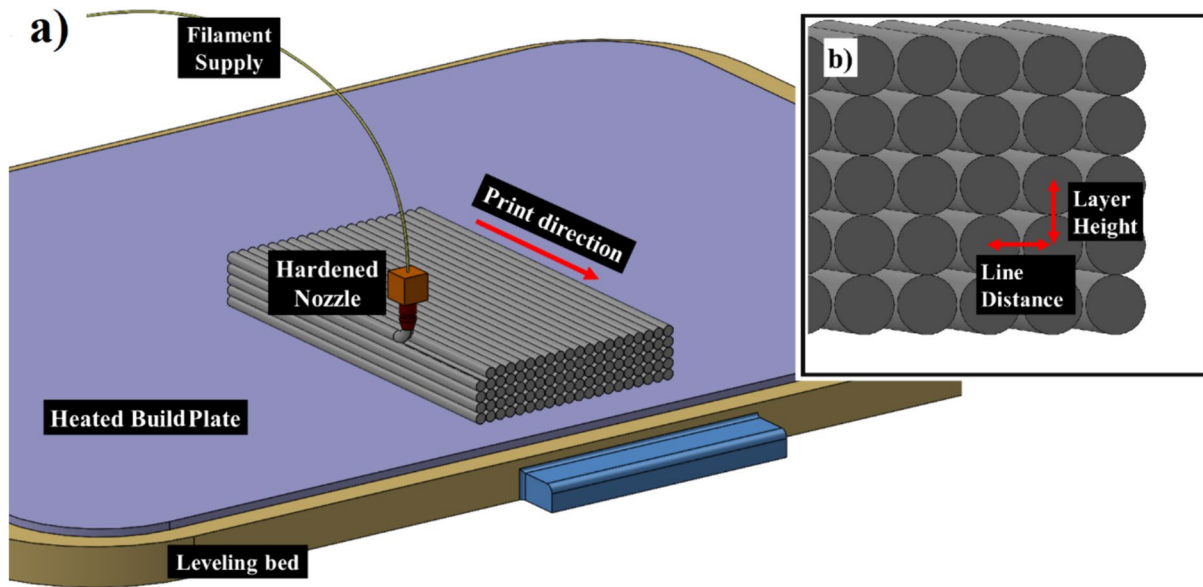


Fig. 2 A schematic representation of the FDM printing process alongside its main parameters

showed that fiber orientation significantly affected the tensile strength, Young's modulus, and flexural strength. In another research [36], the influence of PA's water absorption characteristics was examined in relation to surface and dimensional defects in FDM 3D printing. The study effectively quantified warping in FDM-printed PA parts, identified influential parameters, and recommended additional research on moisture absorption as a relevant parameter for future studies. A similar article studied the effects of printing parameters on the mechanical properties of ABS specimens, reporting the optimal infill, orientation, and layer thickness values [37].

Studies on the effects of the FDM printing parameters on various mechanical properties of the final part, including its impact resistance [38] and tensile strength [39] have emerged as a significant area of interest among researchers. The development of 3D-printed CF composites is progressing rapidly as researchers continuously improve their physical properties and characterize their mechanical responses. An article by Kamaal et al. examined the effects of FDM printing parameters on the mechanical properties of 3D-printed CF-reinforced PLA composite [40]. The optimal values for the building direction, infill percentage, and layer height variables were found using the technique for order of preference by similarity to ideal solution (TOPSIS) analysis for multi-optimization to maximize strength while using the least amount of material. The study reveals that tensile strength is significantly influenced by infill percentage, layer height, and building direction.

A recent study has examined the influence of various matrix materials on the thermal properties of short CF-reinforced composites [21]. Significant variations in thermal characteristics were found among polymers when CF was

Table 1 Invariable parameters in the FDM printing process of short CF-reinforced PA

Parameters	Input
Nozzle diameter	0.4 mm
Nozzle temperature	270 °C
Build bed temperature	100 °C
Shell wall count	2
Shell wall width	0.4 mm
Infill density	100%
Infill pattern	Longitudinal
Infill print direction	0 Degrees
Flow ratio	100%
Maximum volume flow	15 mm ³ /s
Cooling fan	No

added, with PETG showing a fourfold increase in thermal diffusivity compared to nylon's twofold increase. In addition, efforts to characterize 3D-printed composite have led to several FE models. Kagawa et al. developed a numerical simulation method using the Mori–Tanaka theory to predict the tensile strength of randomly oriented short fiber reinforced polymers [41]. Another study refined classical lamination theory-based finite element models to predict elastoplastic and bimodular behavior of 3D-printed composites using short CF-reinforced ABS, demonstrating Hill's yield function effectively predicts stress–strain behavior [42]. Furthermore, understanding the effect of elevated temperatures on the mechanical properties of 3D-printed CFRPs has been the topic of several research articles [7, 43, 45]. It was found that the heat deflection temperature (HDT) of the CFRP was

Table 2 Printing parameters selected for optimization using the Taguchi design method, along with their respective values

Parameter	Factor level			
	Level 1	Level 2	Level 3	Level 4
Infill line distance (mm)	0.3	0.4	0.5	0.6
Layer height (mm)	0.075	0.15	0.22	0.3
Print speed (mm/s)	20	50	75	100
Chamber temperature (°C)	25	35	45	55

lower than the pure PLA matrix agent (65°C), attributed to lower storage modulus.

The increasing use of CF-reinforced polymers in the 3D printing industry has highlighted the need to optimize process parameters for improved structural property performance. However, an examination of the mechanical and microstructural impacts of printing parameters, particularly elevated temperatures, on CF-reinforced plastics remains outstanding. The main objective here is to determine the optimum values for several FDM printing parameters when utilizing chopped CF-reinforced polyamide. The goal of optimization is to maximize the UTS and minimize the inter-layer porosities while also considering the printing time and weight of the part. This study uses the Taguchi method for the DOE. This method is chosen for its robustness in optimizing multiple parameters efficiently. Several tensile test samples were designed according to ASTM D638 type 1 standard and printed using parameters specified by the Taguchi design. Furthermore, cubic samples were printed with print parameters similar to tensile test specimens. The porosities in the cross-sections of these cubic samples were estimated using optical micrography and ImageJ software for image processing. Using the Taguchi model, the optimal values for the printing parameters are determined and presented according to several criteria, including “maximum tensile strength,” “minimum porosity,” and “maximum UTS/weight & UTS/time.”

2 Material and method

2.1 Material

Reinforced polymer filaments typically contain 15 ± 5 wt.% of carbon, in contrast to traditional composite laminates, which contain 50–70% CFs by weight. A 1.75-mm diameter filament (Ultrafuse PAHT CF15, BASF 3D Printing Solutions GmbH) with polyamide (PA) base plastic and 15 wt.% CF was used. The density of the filament was calculated to be 1207 kg/m^3 . Figure 1 illustrates the cross-section of the filament that was used to print specimens. As shown, the fibers of carbon are asymmetrically distributed within

Table 3 The printing properties of test samples determined utilizing the Taguchi method

Sample number	Infill line distance (mm)	Layer height (mm)	Print speed (mm/s)	Chamber temperature (°C)
No. 1	0.3	0.075	20	25
No. 2	0.3	0.15	50	35
No. 3	0.3	0.225	75	45
No. 4	0.3	0.3	100	55
No. 5	0.4	0.075	50	45
No. 6	0.4	0.15	20	55
No. 7	0.4	0.225	100	25
No. 8	0.4	0.3	75	35
No. 9	0.5	0.075	75	55
No. 10	0.5	0.15	100	45
No. 11	0.5	0.225	20	35
No. 12	0.5	0.3	50	25
No. 13	0.6	0.075	100	35
No. 14	0.6	0.15	75	25
No. 15	0.6	0.225	50	55
No. 16	0.6	0.3	20	45

the cross-section of the filament. The fibers have an average length of $100 \pm 50 \mu\text{m}$ and a diameter of $7 \pm 0.5 \mu\text{m}$. The limited diameter of these filaments, typically ranging from 0.2 to 0.6 mm, allows them to flow through the nozzles of the FDM printers without obstructing the path or wearing out the nozzle’s internal components due to the abrasive nature of carbon particles [46]. Before use, the CF-reinforced PA filament roll was placed in a dryer at 85° C for 12 h. This process, recommended by the filament supplier, reduced the material’s humidity.

2.2 FDM printing

The FDM printing process involves extruding thermoplastic filament layer-by-layer through a heated nozzle, melting the material, and depositing it according to the patterns provided by the user in the G-code. Figure 2 illustrates the schematic process of FDM printing and its related parameters. As shown in Fig. 2a, the filament roll is placed inside or near the printer (usually inside a dry box) and fed to the heating section using a set of mechanical gears placed above the nozzle. The filament is then heated to a predefined temperature, and the semi-molten material is pushed through the nozzle and deposited on top of the previous layer. In this study, the Sermoon D3 pro printer from Creality3D was used to fabricate the tensile and porosity samples. The nozzles of this machine are made from hardened steel and can withstand abrasive filaments such as CF-reinforced polymer. Moreover, the integrated heating chamber enables the investigation of the impact of elevated ambient temperatures on

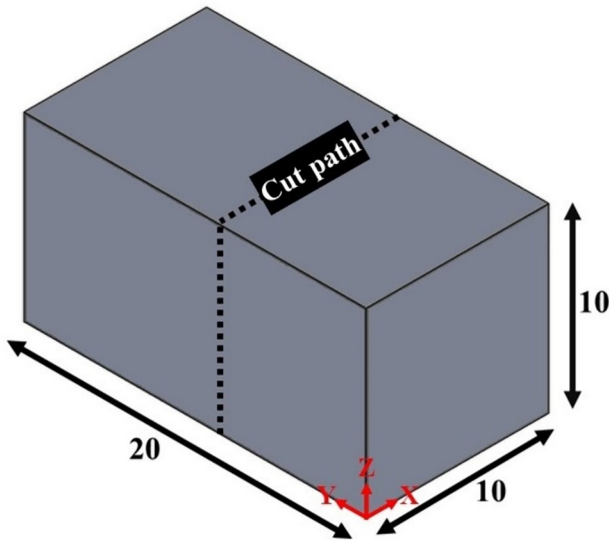


Fig. 3 The geometry of the 3D-printed samples utilized for porosity analysis (dimensions are in mm)

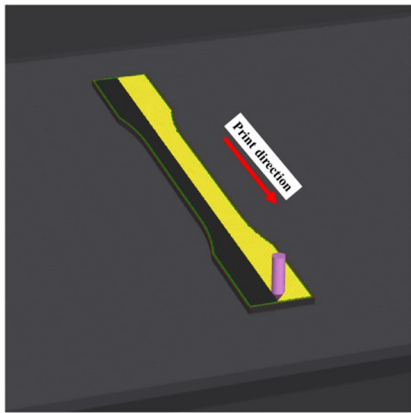
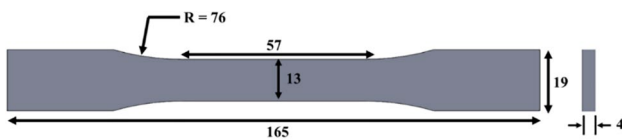


Fig. 4 Geometry of the test sample designed according to ASTM D638 type 1 standard (dimensions in mm), with the printing direction relative to the specimen

the mechanical and microstructural properties of the printed material.

Several printing parameters, including the build plate and nozzle temperatures, have been assumed to remain constant for all printed samples. All the specimens for the tensile test and porosity analysis were printed along the 0° longitudinal direction with an infill density chosen to be 100%. This enables the examination of the material's mechanical properties without the need to address the effects of diverse infill

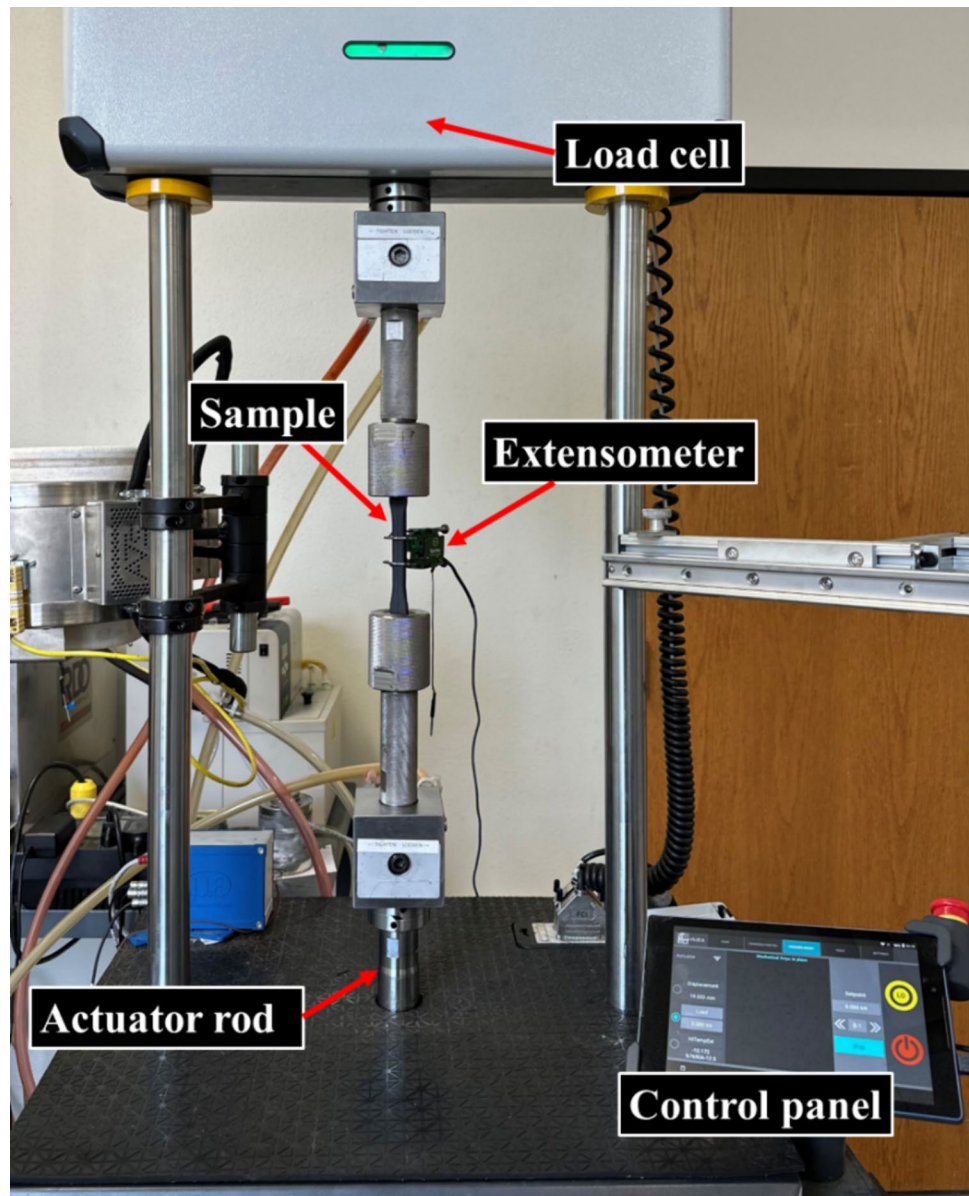
densities and infill patterns (such as grids, triangles, honeycomb, etc.) on the mechanical characteristics of 3D-printed samples. Table 1 summarizes the specifications of the printer along with the constant printing parameters.

2.3 Taguchi design

In addition to the fixed printing parameters mentioned earlier, certain parameters with variable values must be determined during the FDM printing process. This study focuses on investigating four main printing parameters: (1) infill line distance, (2) layer height, (3) print speed, and (4) chamber temperature. The objective is to find the optimized values for these parameters so that the printed specimen achieves the highest UTS, contains the lowest porosity, or obtains the maximum value for the combination of strength-to-print time and strength-to-print weight. While maximum strength and minimum porosity are desirable targets, various applications require balancing these with print time and weight, particularly in industries like aerospace and automotive. Table 2 displays the values selected for each parameter within the limits set by the printer and filament providers. According to the table, a total of $4^4 = 256$ specimens are required to be analyzed to cover all the parameter combinations. Thus, the Taguchi method is employed here to minimize the number of specimens needed to identify the optimal values for these parameters. This approach has been previously applied in mechanical design tasks and demonstrated its capability to yield favorable outcomes [47, 48].

Three steps that make up the Taguchi method are DOE, analysis of the signal-to-noise (S/N) ratio, and optimization. In the DOE phase, a sequence of experiments is established to gain insights into how various factors influence the functioning of the process. The Taguchi method employs orthogonal arrays to organize experiments and signal-to-noise (S/N) ratios to evaluate quality features, determine their significance, and assess the impact of the elements. These arrays consist of systematically organized test cases, enabling a quick and accurate determination of the most significant factors. Orthogonal arrays reduce the required number of experiments by ensuring that each factor is tested at a different level. Each experiment's performance is assessed in the S/N ratio analysis step by comparing the signal, or desired output, to the noise or undesired output. The S/N ratio is employed to ascertain the optimized value of each parameter. The optimization process includes employing the S/N ratio analysis to determine the optimum quantity of each element and running validation trials to verify the findings [32, 49]. The formulation of the Taguchi method for calculating the S/N ratio differs depending on the optimization goal, i.e., minimizing or maximizing the output. In cases where

Fig. 5 The tensile testing machine and its principal components, employed for evaluating the mechanical properties of CFRPs in accordance with the ASTM D638 standard



maximizing the product parameter is advantageous, as is the objective of this article, the formula for S/N is [50]:

$$S/N_i = -10 \log \left(\frac{1}{N_i} \sum_{u=1}^{N_i} \frac{1}{y_u^2} \right) \quad (1)$$

Here i is the run (specimen) number, N_i is the number of experimental runs, and y_u is the response for the u th experiment. Using the Taguchi method in Minitab software with 4 factors and 4 levels, the L16 test design was selected and the number of specimens was reduced from 256 to 16. The values for the four parameters stated above are presented in Table 3 for all 16 specimens of the Taguchi design. These parameters are then utilized in the slicer software to define the specific printing properties for each specimen.

2.4 Porosity estimation

Voids and porosities affect the mechanical properties of the final printed component [51]. Porosities are usually caused by either an incorrect selection of layer height and print line distance or the presence of humidity within the filament, which evaporates during the printing process and leaves a hollow cavity within the printed material [52]. Depending on the printing parameters and the quality of the filament, voids can account for up to 25% of the final volume of the printed specimen [51]. To analyze porosity, 16 samples with dimensions of $1 \times 1 \times 2$ mm, as shown in Fig. 3, were printed using the experimental sequence and printing parameters given in the L16 array Taguchi design in Table 3. Specimens were cut along the XZ plane using a 0.3 mm thick saw blade

Table 4 Printing time and weights of the tensile test samples printed using Taguchi design parameters

Sample number	Print time (min)	Weight (g)
No. 1	429	14.86
No. 2	88	13.39
No. 3	52	13.83
No. 4	31	12.56
No. 5	152	13.06
No. 6	165	12.72
No. 7	34	13.16
No. 8	31	13.17
No. 9	94	10.97
No. 10	40	10.94
No. 11	102	11.50
No. 12	38	11.47
No. 13	71	10.07
No. 14	44	10.15
No. 15	45	10.59
No. 16	76	10.65

and polished with a fine-grade sanding disc to reveal the cross-section. Using a digital integrated microscope, three microscopic images, each covering an area of 2×2 mm were taken from different sectors of the cross-section of each specimen. Subsequently, using the image processing software ImageJ, the porosity of each specimen was calculated by averaging the porosity values from three images.

2.5 Tensile tests

The design of the tensile test specimens followed the ASTM D638 Type 1 standard, resulting in samples that are 165 mm in length and 4 mm in thickness. The design was then imported into slicing software, where the printing parameters listed in Table 3 were assigned to each specimen before printing. Figure 4 illustrates the geometry of the samples designed according to the ASTM D638 Type 1 standard. Additionally, this figure indicates the printing direction relative to the specimen.

An axial fatigue testing machine (910 series, TestResources, Inc.) with a load capacity of 25 kN was employed to perform the tensile experiments. The grip length for tensile samples was set at 25 mm, as directed by the standard, and the displacement rate for the tensile test was maintained at 0.02 mm/s for all samples. An extensometer was used during testing to accurately measure the strain values. Data was recorded at the rate of 250 points per second. The primary components of the tensile test apparatus are displayed in Fig. 5. The Young's modulus (EII) and UTS were determined for each specimen. Tensile tests were repeated if the

specimen's break point occurred outside the gauge section area.

3 Results and discussion

Table 4 presents the printing time and actual weights of the L16 design specimens. Referring to Table 3, specimen No. 1 has the longest printing time, nearly 14 times greater than samples No. 4 and No. 8. By comparing the specimens' parameters with the corresponding times, it is revealed that the print speed and layer height are together the most important variables determining the total print duration. In addition, samples No. 1 and No. 13 have the largest weight difference, equal to 47%. This discrepancy primarily arises from variations in extrusion line distance or layer height among samples, leading to dissimilar deposition of the extruded material within the layers. Therefore, given these calculations, it is evident that specimens with a 100% infill density can exhibit different densities if other printing parameters vary.

To determine the precise orientation of chopped CFs within the printed specimens and to assess if this orientation is aligned with the 0° print infill pattern, several samples with the "line" infill pattern and along the 0° direction were printed using the CF-reinforced PA filament and examined using an SEM device. Figure 6 shows Scanning Electron Microscope (SEM) images taken from (a) the specimens' top surface and (b) their cross-sections. The SEM images were obtained with an accelerating voltage (HV) of 5.0 kV, a working distance (WD) of 10–11 mm, and an Everhart–Thornley Detector (ETD). From images, most fibers fall in the 50–100 μm length range. From these images, it is evident that the majority of fibers, with lengths ranging from 50 to 100 μm , are aligned in the same direction as the extruded material.

3.1 Mechanical properties

The results of the tensile experiments conducted on the 16 specimens are presented in Figs. 7 and 8. Based on these graphs, the tensile strength of the specimens varies between 72.1 MPa for specimen No. 14 and 171.8 MPa for sample No. 1, with an average of 115.7 MPa across all specimens. Comparing this value with the UTS of unreinforced high-temperature PA, which equals 75.6 MPa, indicates the noticeable improvement in tensile properties due to CF reinforcement.

In general, the combination of matrix and fibers increases structural performance, resulting in composites with a greater resistance to failure than monolithic polymers. This is primarily achieved by increasing the material's fracture

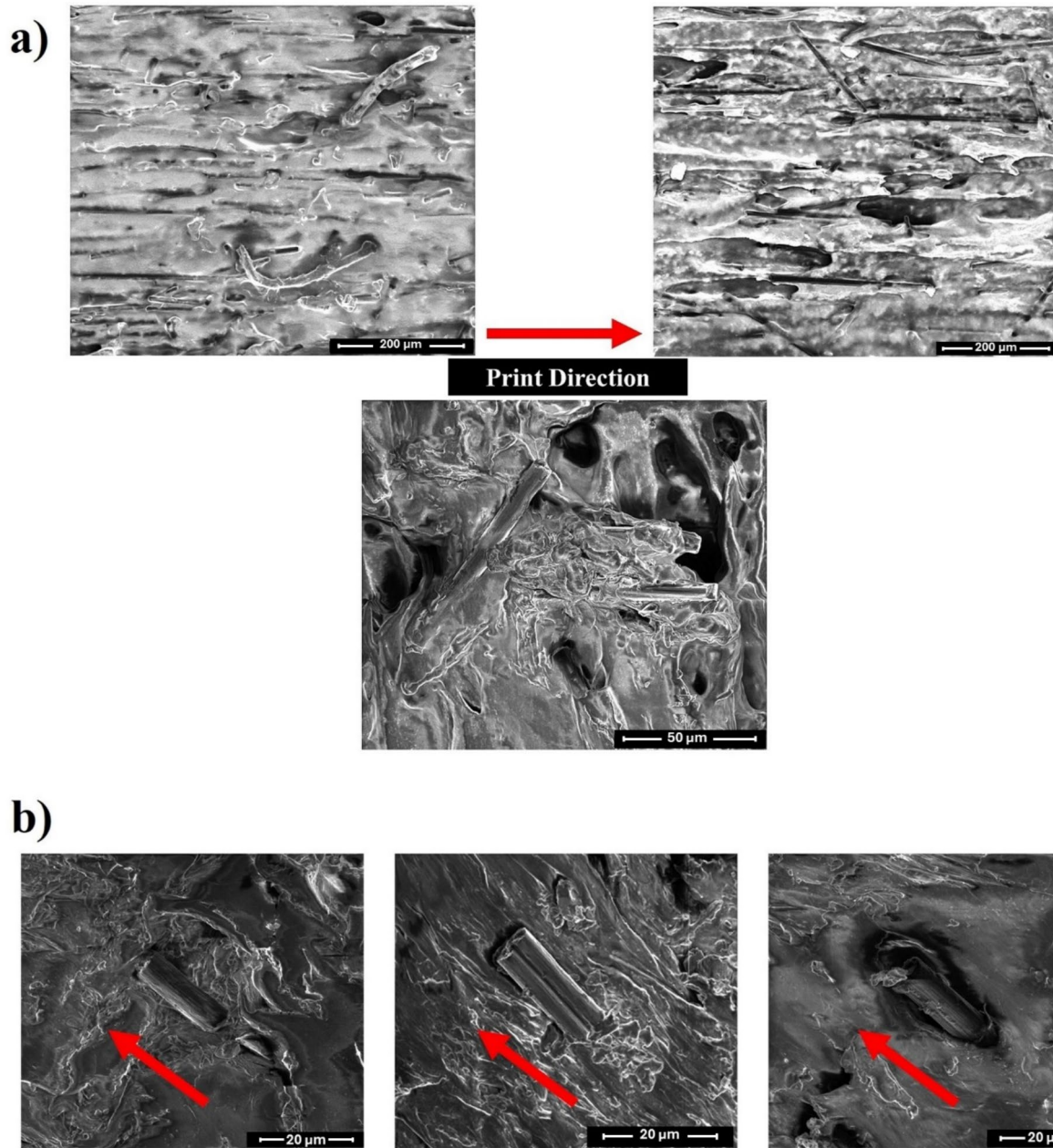


Fig. 6 SEM images depicting **a** the printed surface and **b** the cross-section of the chopped CF-reinforced polymer. The fiber orientation is discernible in section **b**

energy through mechanisms such as crack deflection, fiber pullout, and stress transfer [53]. All tested specimens displayed brittle behavior under tensional loading, characterized by a lack of discernible yield point or plastic deformation before failure. Exceptions were observed in specimens No. 2 and No. 4, which exhibited a brief plastic phase and break strains greater than 1.8%.

Table 5 shows the calculated UTS and failure strain (elongation at breakage) for all 16 specimens. Comparing the estimated e_f with the average elongation at fracture

of Polyamide (~40% [54]) highlights how reinforcement enhances the stiffness of the material and lessens its ability to deform before failure. The UTS values presented in this table will later be used in the analysis of Taguchi design to find the optimal printing parameters for chopped CF-reinforced polymers.

The optimization of these 16 specimens can be conducted using various metrics. One possible approach is to concentrate solely on the UTS and determine the optimal parameter that yields the highest UTS. Another method

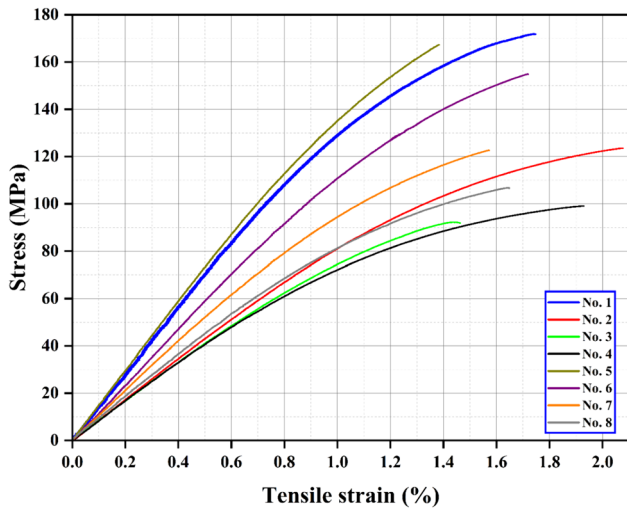
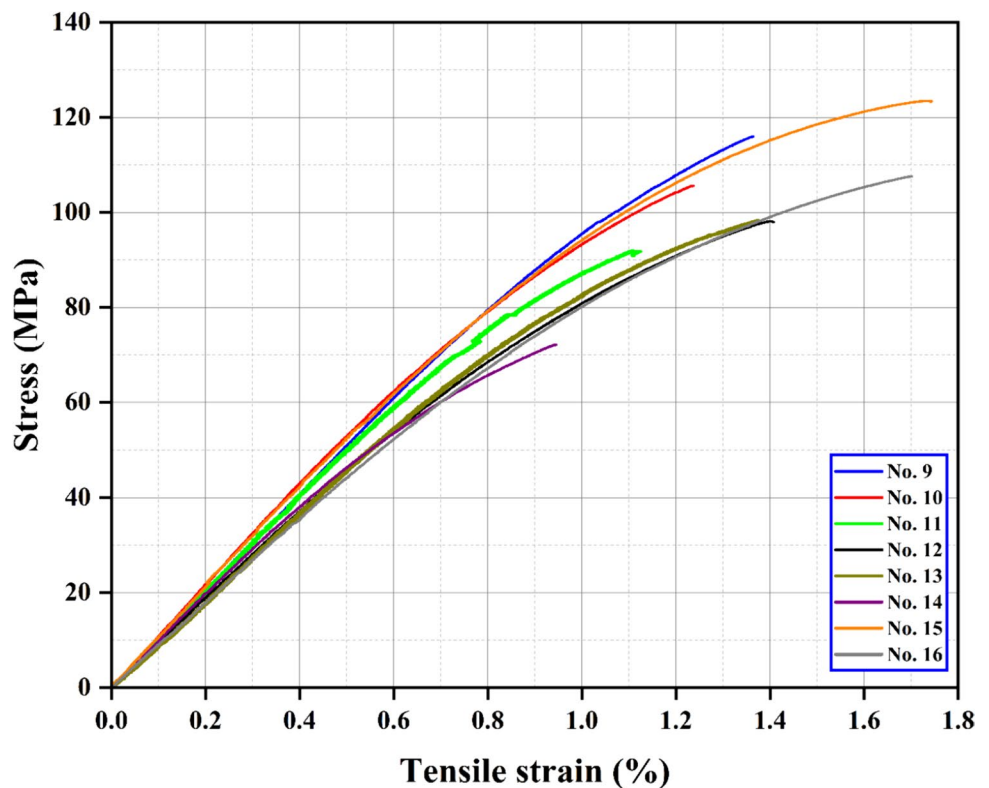


Fig. 7 Tensile stress–strain behavior of specimens No. 1 to No. 8

involves considering the weight of the samples and their printing time, specifically by choosing the maximized UTS/weight and UTS/time ratios as the optimization objective. Figure 9 compares the samples by considering the measures stated above. All values are normalized to enhance the coherence of the graph using min–max normalization, assuming a minimum value of 0 for all cases. The graph indicates that specimens No. 1, No. 5, and No. 6 demonstrate superior tensile strength; however, their

Fig. 8 Tensile stress–strain behavior of specimens No. 9 to No. 16



performance in terms of UTS/print time is comparatively weaker than that of other samples. For example, the UTS/print time ratio for specimen No. 7 exceeds that of sample No. 1 by more than 9 times. Similar trends can be observed for the UTS/weight ratio. The purpose of comparing these parameters is to improve the accuracy of Taguchi analysis. In numerous applications, the strength-to-weight ratio is more important than strength alone. In addition, in manufacturing practices, production time is a critical factor to consider.

A comparison between the Young’s modulus (E_{11}) values of these 16 tensile samples is shown in Fig. 10. According to this figure, while the stiffness values for most samples are similar, specimens No. 1 and No. 5 exhibit relatively higher stiffnesses. In contrast, specimens No. 3 and No. 4 fall on the lower end of the range, with stiffnesses approximately equal to $0.5E_{11}$ of sample No. 1. An analysis of these values using the Taguchi method reveals that layer height has the most significant impact on the E_{11} results, with a layer height of 0.075 mm yielding the highest stiffness, followed by print speed. Furthermore, while chamber temperature had the least importance on the outcome, a chamber temperature of 25 °C resulted in the highest stiffness, which decreased with increasing temperature. This highlights how altering the printing parameters can significantly affect the microstructural properties of the printed part. The average E_{11} of 9.55 GPa, calculated based on these 16 specimens, is relatively close to the 8.38 GPa reported by the filament supplier.

Table 5 Ultimate tensile strength and elongation at fracture for 16 specimens tested according to Taguchi design parameters

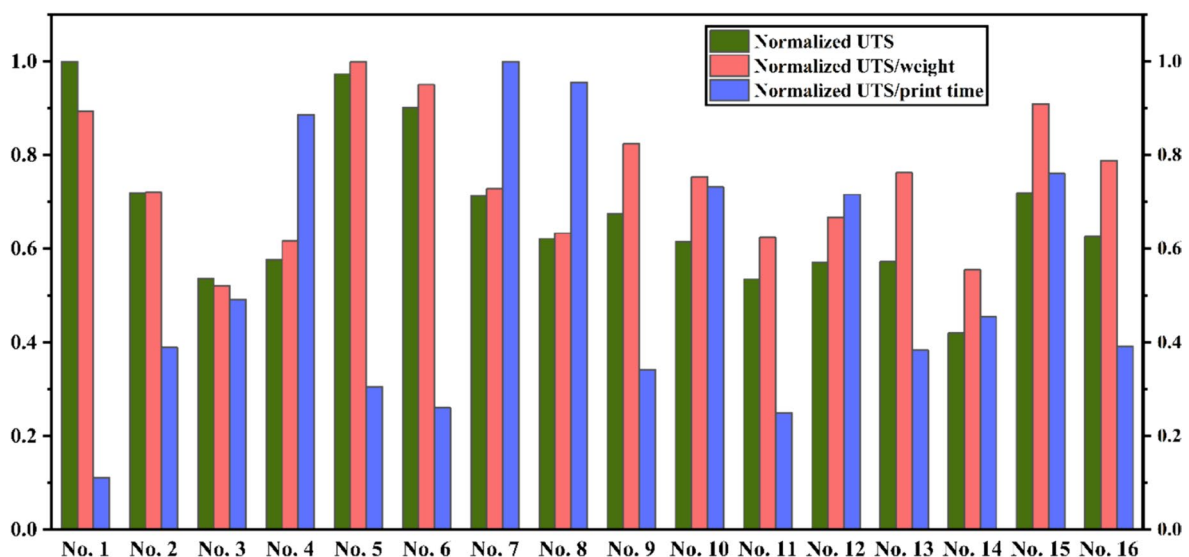
Sample number	UTS (MPa)	e_f (%)
No. 1	171.86	1.741
No. 2	123.54	2.076
No. 3	92.22	1.463
No. 4	99.09	1.929
No. 5	167.30	1.382
No. 6	154.90	1.719
No. 7	122.65	1.571
No. 8	106.83	1.647
No. 9	115.99	1.363
No. 10	105.62	1.235
No. 11	91.93	1.110
No. 12	98.12	1.408
No. 13	98.35	1.369
No. 14	72.16	0.904
No. 15	123.50	1.741
No. 16	107.60	1.700

An example of a post-failure tensile test specimen is presented in Fig. 11. Figure 11a illustrates the failure section of specimen No. 4, and Fig. 11b, c show the microscopic images of the fracture cross-section and fracture surface (edge), respectively. Two primary modes of fracture in 3D-printed composites are depicted in these images. Delamination between adjacent layers in Fig. 11b and fiber pull-out in Fig. 11c are among the main failure mechanisms in fiber-reinforced composites.

3.2 Porosity assessment

Figure 12 presents SEM images illustrating the cross-sections of the samples with the four different layer heights investigated in this work. From the images, in the specimen with a layer height of 0.075 mm, the printed layers are fully adjacent, with minimal inter-layer porosities. Conversely, discernible pores between the layers are detectable in samples with layer heights of 0.22 mm and 0.3 mm. The porosities within the printed parts not only serve as stress concentration points leading to uneven stress distribution and premature failure but also reduce the effective cross-section of the material, consequently diminishing its strength. A higher inter-layer porosity would lead to weaker bonding between layers and increase the likelihood of delamination, particularly under fatigue loading conditions.

As previously mentioned, cubic samples were 3D printed according to the L16 design parameters outlined in Table 3. The porosities within the cross-sections of these samples were subsequently calculated using the ImageJ software. Figure 13 demonstrates the porosity measurement process using this software. The pores, initially detectable as black regions in the first image, are highlighted in red in the second image. The percentage of this highlighted area relative to the entire surface area is then calculated to determine the porosity. Threshold adjustments were performed on ImageJ during each sample's three measurements to ensure an accurate selection of the porosity area for area ratio measurement. Figure 14 presents the porosity estimations for the three regions of each sample, along with their average values. From this figure, specimen No. 1 displayed the lowest porosity of 1.44%, mainly attributed to its small layer height and infill line distance values. The observed porosity type in

**Fig. 9** A comparison between the normalized values of UTS, UTS/sample weight, and UTS/print time for Taguchi design tensile samples

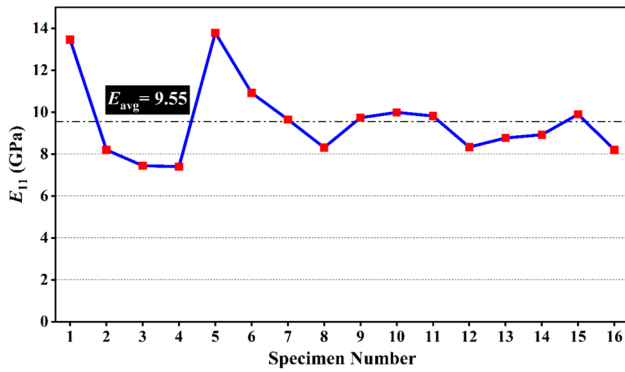


Fig. 10 Comparison of the calculated Young's Modulus (E_{11}) values for 16 tensile specimens of Taguchi design

this sample was intra-layer pores, which are cavities within the extruded material, as opposed to gaps between print lines or layers. On the other hand, samples with higher porosities, particularly those exceeding 10%, exhibited hollow spaces between adjacent layers as well as in the infill lines within each layer. Notably, samples No. 15 and No. 16 exhibited visible interlayer pore spaces. These findings also explain the weight discrepancies among samples despite their similar geometries. From this figure, significant variations (1.4% compared to 17.6%) exist in the porosity of the 16 specimens. Initially, there is a sharp rise in porosity, peaking at over 12% for sample No. 4. This increase is precisely aligned

with the increase in layer height in samples No. 1 to No. 4. Following this peak, porosity decreases significantly to 3%, as the layer height for sample No. 5 is 0.075 mm and the porosity rises again as the layer height increases. The overall upward trend can be attributed to the increase in infill line distance within each set of four samples. These observations suggest that both layer height and infill line distance affect the porosity inside the 3D-printed sample, with higher values of these properties leading to higher porosities.

3.3 Taguchi design analysis

The objective here is to determine the maximum value for the target parameter, which could be solely the tensile strength or a combination of UTS/sample weight and UTS/print time, or to determine the minimum value for porosity. Depending on the optimization goal, i.e., to decide whether the intended outcome is to maximize UTS or minimize porosity, the data needs to be analyzed separately in Minitab.

Figure 15 illustrates the results of the Taguchi design analysis, assuming that the objective is to (a) maximize the UTS and (b) minimize the porosity. When using the Taguchi method in Minitab for parameter optimization, two key graphs are generated: the "Main effects plot for means," showing how average responses (e.g., UTS, porosity) change with parameter levels, and the "main effects plot for SN ratios," illustrating the robustness of the process by displaying the signal-to-noise ratios at each parameter level.

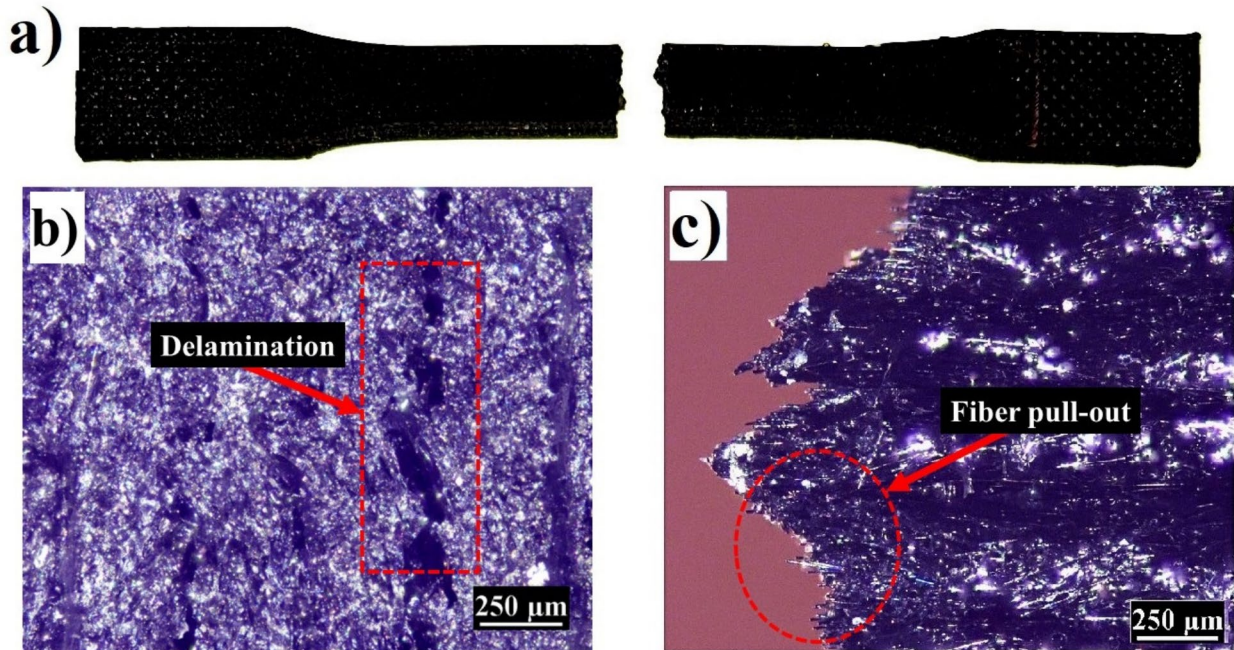


Fig. 11 The tensile test specimen No. 4 post-failure. a depicts the failure location of the specimen, b shows an optical microscopic image of the fracture cross-section, and c displays the fracture surface (edge)

Fig. 12 SEM images from the samples with different layer heights of 0.075, 0.15, 0.225, and 0.3 mm

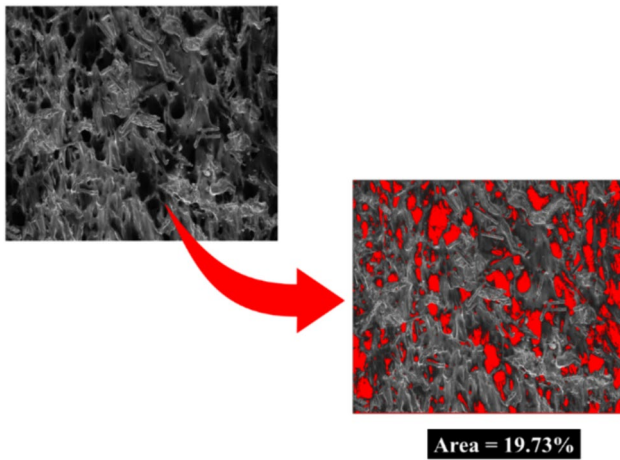
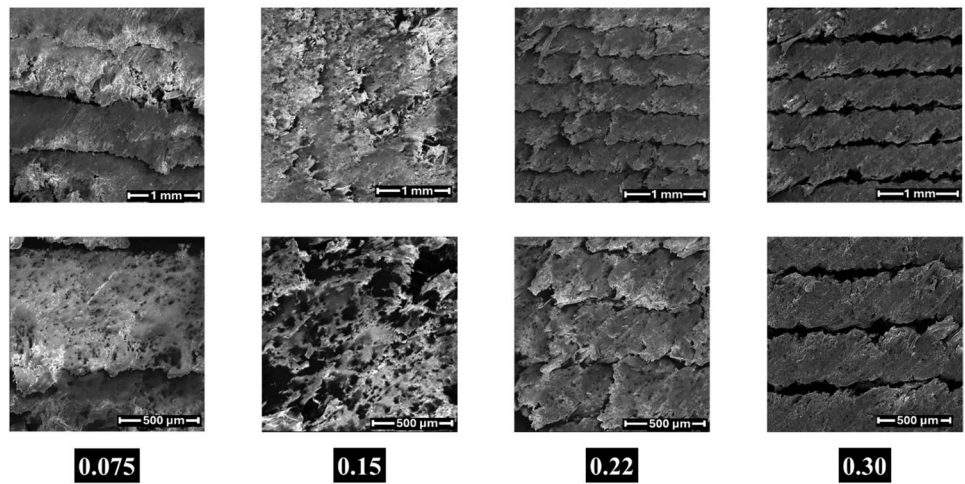


Fig. 13 A schematic diagram illustrating the process of porosity calculation using ImageJ software

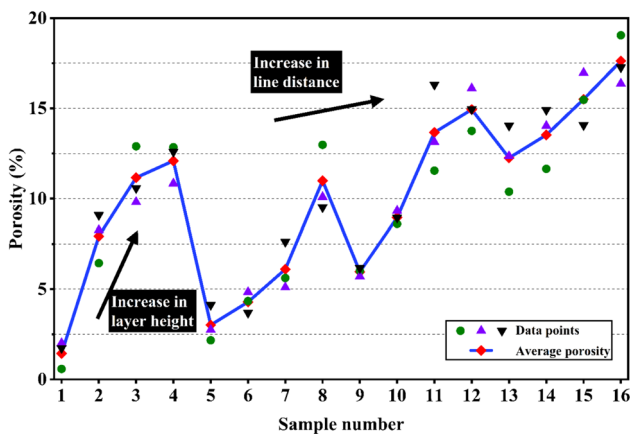


Fig. 14 Comparison of porosities between 16 specimens fabricated using Taguchi design parameters

Figure 15a reveals that UTS drops with increasing the infill line distance, layer height, and printing speed. However, It increases as the chamber temperature is increased. The layer height and infill line distance are directly related to the inter-layer and intralayer bonding in the part and significantly influence the UTS; In addition, as the print speed increases, the likelihood of disconnected print lines also increases, leading to higher stress intensities. The S/N ratios graph suggests that the optimal values for the printing parameters with this objective are as follows: “Infill line distance” = 0.4 mm, “Layer Height” = 0.075 mm, “Print Speed” = 20 mm/s, and “Chamber temperature” = 55 °C. With these printing parameters, the predicted value for UTS according to the Taguchi model is 185 MPa.

Figure 15b shows the outcomes of the Taguchi analysis with the objective of minimum porosity. According to the Means plot, as expected, a steady increase in porosity is detectable with the increase in layer height. For the infill line distance, the most optimal value appears to be 0.4 mm, resulting in the lowest porosity, whereas a value of 0.3 mm leads to an overflow of the extruded material, negatively affecting the intralayer porosity. As indicated, the other two parameters have lesser effects on the porosity of the material. From the SN ratio graph, the optimal values for the printing parameters of infill line distance, layer height, print speed, and chamber temperature are 0.4 mm, 0.075 mm, 20 mm/s, and 25 °C accordingly for the minimum porosity. Based on the Taguchi prediction, the printed sample with these parameters exhibits a porosity ratio of only 0.25%. An additional optimization targeting both maximum UTS and minimum porosity as simultaneous objectives yields printing parameters identical to those optimized for maximum UTS alone. The analogous variations in UTS and density percentage (calculated as 100% minus porosity) across the specimens, as illustrated in Figs. 9 and 14, substantiate this outcome.

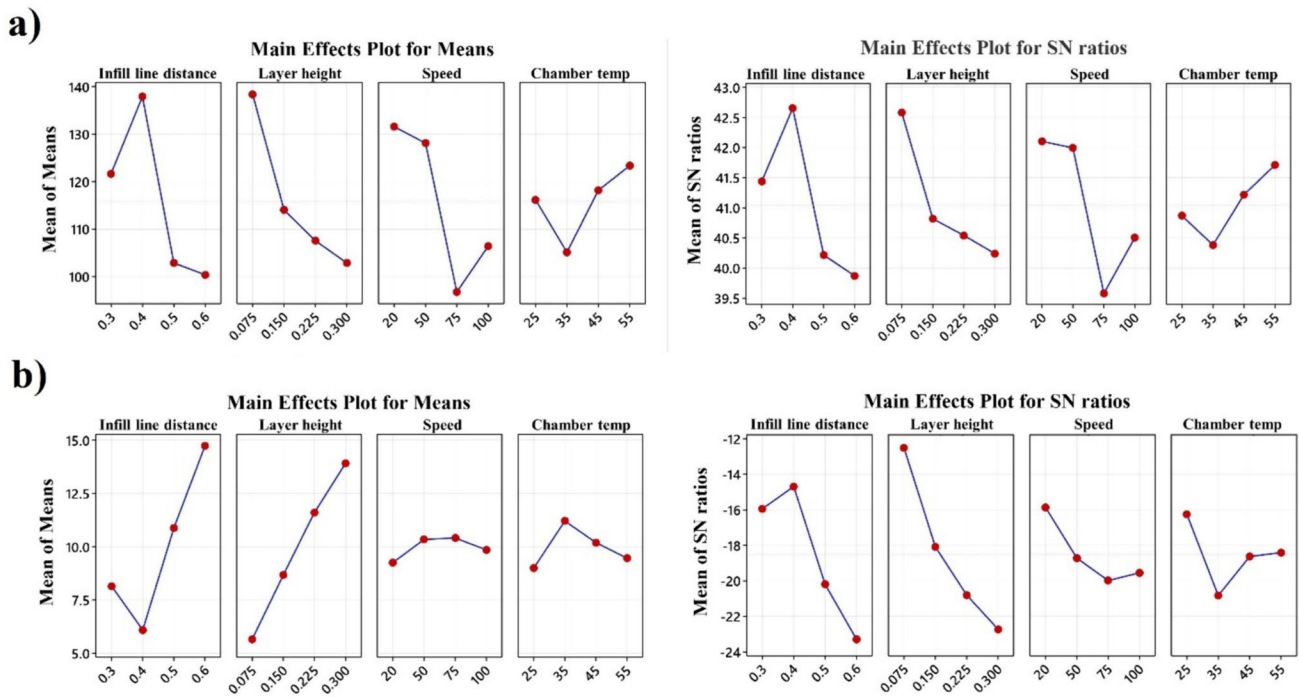


Fig. 15 Taguchi design results, considering the objective is to achieve **a** maximum UTS or **b** minimum porosity

Ultimately, the Taguchi optimization is performed using the Ultimate Tensile Strength (UTS), sample weight, and print time data of the L16 specimens. The objective is to maximize the values of UTS/sample weight and UTS/printing time simultaneously. To do so, normalized values of these two parameters were used in the Minitab. Figure 16 depicts the graphs generated using this approach. From the Means graph, although there are no consistent correlations between the variations of each parameter and changes in the objective parameter, in general, an increase in all parameters except for the layer height is favorable. According to the “S/N ratios” graph, the optimal values for infill line distance, layer height, printing speed, and chamber temperature are determined to be 0.4 mm, 0.3 mm, 100 mm/s, and 55 °C, respectively. Based on the Taguchi predictions, the optimized printing properties result in a UTS/weight ratio of 10.202 and a UTS/time ratio of 3.97, which is on average, 12% improved compared to the best specimen among the 16 samples tested earlier for L16 design.

3.4 Verification

Using the optimized values obtained in the previous section with the maximum strength, minimum porosity, and maximum UTS/weight and UTS/time objectives, three specimens were printed and tested to verify the optimization accuracy and compare with the predictions of the Taguchi method. The specimen optimized for the highest UTS had a print

time of 347 min and upon a tensile test, the value for the UTS was calculated to be 179 MPa, a UTS higher than sample No.1 despite having a lower printing time. The sample optimized for the lowest porosity exhibited negligible porosity within its cross-section, as evidenced by the micrography images. This suggests that the primary source of porosity in 3D-printed materials is related to interlayer pores, which can be mitigated by selecting an appropriate set of parameters. Next, the specimen with optimized parameters for the simultaneous maximum UTS/weight and UTS/time ratios was printed and tested in the tensile test machine. The UTS for this specimen was 122.5 MPa, despite a printing time of only 29 min and the weight of 12.29 g. This resulted in the UTS/weight and UTS/time ratios equal to 9.96 and 4.22, respectively. These optimized values agree with the Taguchi model’s predictions and are, on average, higher than all the 16 samples tested earlier for the Taguchi model.

It should be noted that there is a distinction in the order of importance when the optimization goal shifts from maximizing strength to maximizing the ratio of strength to weight and print time. In the strength-focused case, the infill line distance emerges as the most crucial parameter. In contrast, when maximizing the strength-to-weight and print time ratios, the printing speed takes precedence. In both instances, the effects of chamber temperature exhibit the least impact on the outcomes. A summary of this comparison between the Taguchi analysis results is presented in Table 6.

Fig. 16 Taguchi design result, considering the objective of having the maximum value of UTS/print time and UTS/specimen weight. The normal probability plot associated with the test results is also depicted in the figure

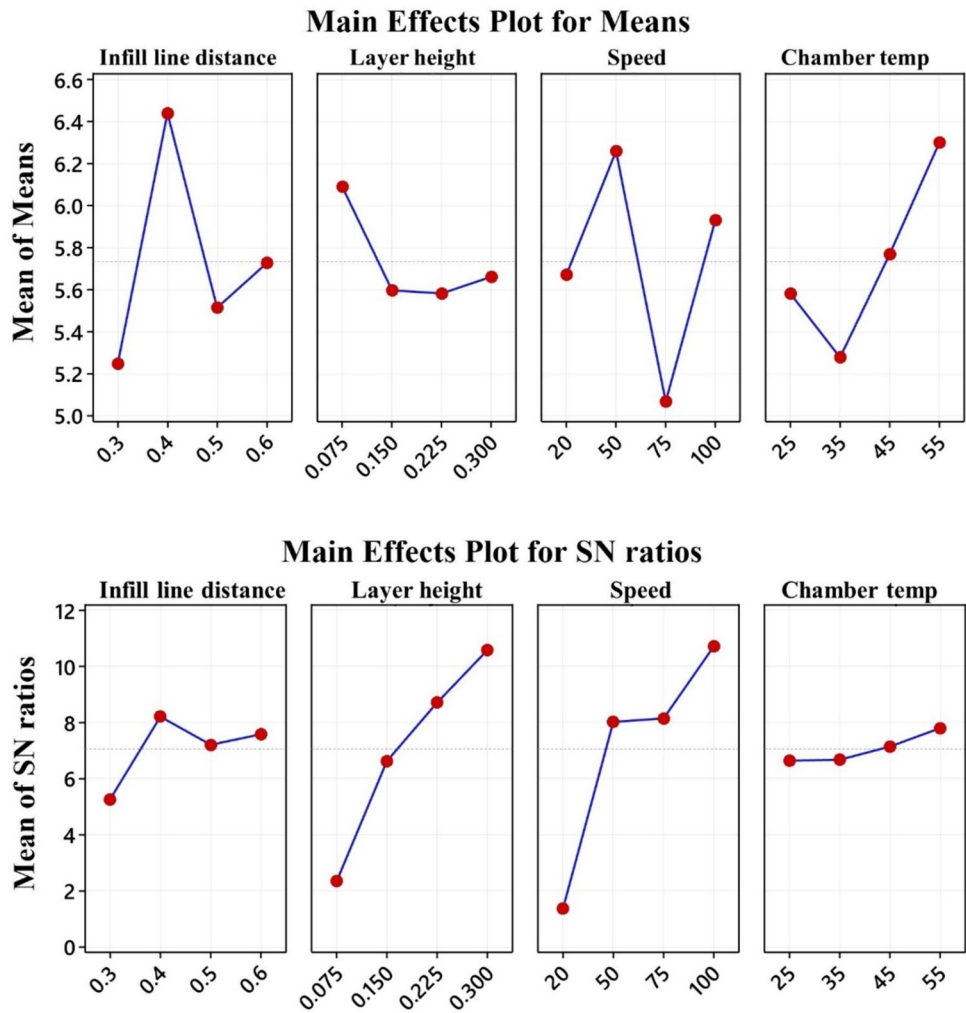


Table 6 Comparison of the results obtained from the Taguchi method for design optimization

Target parameter		Infill line distance (mm)	Layer height (mm)	Print speed (mm/s)	Chamber temperature (°C)	Taguchi prediction	Test result	Error (%)
Strength	Order of importance	1	3	2	4	185 MPa	179.30	-3.1
	Optimal value	0.4	0.075	20	55			
Porosity	Order of importance	2	1	4	3	0.25%	< 1%	-
	Optimal value	0.4	0.075	20	25			
Strength/weight and strength/time	Order of importance	3	2	1	4	10.20	9.96	-2.3
	Optimal value	0.4	0.3	100	55	3.97	4.22	+6.2

4 Conclusions

This study employed the Taguchi method to optimize FDM printing parameters for fabricating chopped CF-reinforced polyamide to maximize the UTS to print time and weight

ratios and minimize the porosity inside the part. The investigated parameters included the infill line distance (0.3–0.6 mm), layer height (0.075–0.3 mm), printing speed (20–100 mm/s), and printing chamber temperature (25–55 °C). Following the L16 Taguchi model, sixteen

tensile test samples were fabricated according to ASTM D638 type 1 standard. All samples were printed with an infill density of 100% and along the 0-degree direction. Moreover, 3D-printed cubic samples with similar properties were printed and used to estimate porosities within the material using optical micrography and ImageJ software. The following conclusions can be drawn:

There was a significant variation in the mechanical properties among the samples. The ultimate tensile strength (UTS) ranged from 72.16 to 171.86 MPa, indicating the influence of printing parameters on material strength. Also, porosity estimations ranged from 1.44% to 17.63%. Optimal printing parameters significantly reduced porosity, enhancing the mechanical integrity of the printed parts.

The optimal parameters for maximizing UTS/print weight and UTS/print time were a 0.4 mm infill line distance, 0.3 mm layer height, 100 mm/s printing speed, and 55 °C chamber temperature.

SEM images showed alignment between the printing direction and fiber orientation. Increased layer height negatively affected interlayer bonding and increased porosity, thereby reducing strength.

Further validation experiments confirmed the reliability of the Taguchi method in predicting optimized parameters.

This study demonstrates that optimizing FDM parameters significantly enhances the mechanical performance of 3D-printed chopped CF-reinforced polymer composites.

Acknowledgements This work was supported in part by the US National Science Foundation, Grant number 2243755.

Funding This study was funded by National Science Foundation, 2243755, Michael Khonsari.

Data availability Data will be provided upon request.

Declarations

Conflict of interest The authors have no competing interests to declare.

References

- Pappas JM, Thakur, AR, Leu MC, Dong X (2021) A parametric study and characterization of additively manufactured continuous carbon fiber reinforced composites for high-speed 3D printing. *Int J Adv Manuf Technol* 113:2137–2151
- Cole DP, Riddick JC, Iftekhar Jaim H, Strawhecker KE, Zander NE (2016) Interfacial mechanical behavior of 3D printed ABS. *J Appl Polym Sci* 133(30)
- Pertuz AD, Díaz-Cardona S, González-Estrada OA (2020) Static and fatigue behaviour of continuous fibre reinforced thermoplastic composites manufactured by fused deposition modelling technique. *Int J Fatigue* 130:105275
- Dev S, Srivastava R (2021) Optimization of fused deposition modeling (FDM) process parameters for flexural strength. *Mater Today Proc* 44:3012–3016
- Desu HPP, Rossi A, Mankoo GK, Fayazbakhsh K, Fawaz Z (2020) Experimental characterization of 3D printed thermoplastic plates subjected to low velocity impact. *Int J Adv Manuf Technol* 107:1659–1669
- Penumakala PK, Santo J, Thomas A (2020) A critical review on the fused deposition modeling of thermoplastic polymer composites. *Compos B Eng* 201:108336
- Soete J, Badoux B, Swolfs Y, Gorbatikh L (2019) Defect detection in 3D printed carbon fibre composites using X-ray computed tomography. In: 9th Conference on Industrial Computed Tomography (iCT), Padova, Italy, p 1–8
- Daher R, Ardu S, di Bella E, Krejci I, Duc O (2022) Efficiency of 3D-printed composite resin restorations compared with subtractive materials: evaluation of fatigue behavior, cost, and time of production. *J Prosthet Dent* 131(5):943–950
- Hou S, Li T, Jia Z, Wang L (2018) Mechanical properties of sandwich composites with 3d-printed auxetic and non-auxetic lattice cores under low velocity impact. *Mater Des* 160:1305–1321
- Rouhi Moghanlou M, Mahmoudi A, Khonsari M, Li G (2024) A comparison of damping-based methods to identify damage to carbon-fiber-reinforced polymers laminates subjected to low-velocity impact. *J Compos Mater* 58(3):401–417
- Mahmoudi A, Mohammadi B (2019) On the evaluation of damage-entropy model in cross-ply laminated composites. *Eng Fract Mech* 219:106626
- Isobe T, Tanaka T, Nomura T, Yuasa R (2018) Comparison of strength of 3D printing objects using short fiber and continuous long fiber. In: IOP Conference Series: Materials Science and Engineering. IOP Publishing
- Ferreira I, Vale D, Machado M, Lino J (2019) Additive manufacturing of polyethylene terephthalate glycol/carbon fiber composites: an experimental study from filament to printed parts. *Proc Inst Mech Eng Part L J Mater Design Appl* 233(9):1866–1878
- Brenken B, Barocio E, Favalaro A, Kunc V, Pipes RB (2018) Fused filament fabrication of fiber-reinforced polymers: a review. *Addit Manuf* 21:1–16
- Wickramasinghe S, Do T, Tran P (2020) FDM-based 3D printing of polymer and associated composite: a review on mechanical properties, defects and treatments. *Polymers* 12(7):1529
- Wang F, Wang G, Wang H, Fu R, Lei Y, He J (2023) 3D Printing technology for short-continuous carbon fiber synchronous reinforced thermoplastic composites: a comparison between tow prepreg extrusion and in situ impregnation processes. *Chin J Mech Eng Addit Manuf Front* 2(3):100092
- Melenka GW, Cheung BK, Schofield JS, Dawson MR, Carey JP (2016) Evaluation and prediction of the tensile properties of continuous fiber-reinforced 3D printed structures. *Compos Struct* 153:866–875
- Dou H, Cheng Y, Ye W, Zhang D, Li J, Miao Z, Rudykh S (2020) Effect of process parameters on tensile mechanical properties of 3D printing continuous carbon fiber-reinforced PLA composites. *Materials* 13(17):3850
- Sanei SHR, Popescu D (2020) 3D-printed carbon fiber reinforced polymer composites: a systematic review. *J Compos Sci* 4(3):98
- Rezaei F, Yunus R, Ibrahim N (2009) Effect of fiber length on thermomechanical properties of short carbon fiber reinforced polypropylene composites. *Mater Des* 30(2):260–263
- Huseynov O, Hasanov S, Fidan I (2023) Influence of the matrix material on the thermal properties of the short carbon fiber reinforced polymer composites manufactured by material extrusion. *J Manuf Process* 92:521–533

22. Ramachandran K, Nasr Azadani M, Ravichandran P, Shivaprakash NB, Obi M, Gnanasagaran CL (2024) Failure mechanics of fused filament fabricated nylon/carbon-reinforced composites. In: Progress in additive manufacturing, pp 1–9
23. Moghanlou MR, Khonsari M (2022) On the kinetic formulation of fracture fatigue entropy of metals. *Fatigue Fract Eng Mater Struct* 45(2):565–577
24. Azizian-Farsani E, Ghodsiyeh D, Akbarzadeh S, Khonsari MM (2020) Theoretical and experimental analysis of relation between entropy and tension–compression fatigue of aluminum 6061–T6. *J Braz Soc Mech Sci Eng* 42:1–10
25. Moretini G, Palmieri M, Capponi L, Landi L (2022) Comprehensive characterization of mechanical and physical properties of PLA structures printed by FFF-3D-printing process in different directions. *Prog Addit Manuf* 7(5):1111–1122
26. Yavas D, Zhang Z, Liu Q, Wu D (2021) Fracture behavior of 3D printed carbon fiber-reinforced polymer composites. *Compos Sci Technol* 208:108741
27. Almeshari B, Junaedi H, Baig M, Almajid A (2023) Development of 3D printing short carbon fiber reinforced polypropylene composite filaments. *J Market Res* 24:16–26
28. Lobov E, Dobryднеva A, Vindokurov I, Tashkinov M (2023) Effect of short carbon fiber reinforcement on mechanical properties of 3D-printed acrylonitrile butadiene styrene. *Polymers* 15(9):2011
29. Monticeli FM, Neves RM, Ornaghi Jr HL, Almeida Jr JHS (2021) A systematic review on high-performance fiber-reinforced 3D printed thermoset composites. *Polym Compos* 42(8):3702–3715
30. Lee S-H, Lim J-K, Nam G, Roh J-S (2023) Changes in mechanical properties of graphite blocks fabricated using natural graphite as a filler by adding 3-mm chopped carbon fiber. *Fibers Polym* 24(6):2083–2091
31. Hikmat M, Rostam S, Ahmed YM (2021) Investigation of tensile property-based Taguchi method of PLA parts fabricated by FDM 3D printing technology. *Results Eng* 11:100264
32. Kargar E, Ghasemi-Ghalebahman A (2023) Experimental investigation on fatigue life and tensile strength of carbon fiber-reinforced PLA composites based on fused deposition modeling. *Sci Rep* 13(1):18194
33. Almeida Jr JHS, Jayaprakash S, Kolari K, Kuva J, Kukko K, Partanen J (2024) The role of printing parameters on the short beam strength of 3D-printed continuous carbon fibre reinforced epoxy-PETG composites. *Compos Struct* 337:118034
34. Monticeli FM, Neves RM, Ornaghi Jr HL, Almeida Jr JHS (2022) Prediction of bending properties for 3D-printed carbon fibre/epoxy composites with several processing parameters using ANN and statistical methods. *Polymers* 14(17):3668
35. Ahmad MN, Ishak MR, Mohammad Taha M, Mustapha F, Leman Z, Anak Lukista DD, Irianto, Ghazali I (2022) Application of taguchi method to optimize the parameter of fused deposition modeling (FDM) using oil palm fiber reinforced thermoplastic composites. *Polymers* 14(11):2140
36. Amithesh S, Shanmugasundaram B, Kamath S, Adhithyan S, Murugan R (2023) Analysis of dimensional quality in FDM printed nylon 6 parts. In: Progress in additive manufacturing, pp 1–14
37. Ahmad MN, Yahya A (2023) Effects of 3D printing parameters on mechanical properties of ABS samples. *Designs* 7(6):136
38. Patterson AE, Pereira TR, Allison JT, Messimer SL (2021) IZOD impact properties of full-density fused deposition modeling polymer materials with respect to raster angle and print orientation. *Proc Inst Mech Eng C J Mech Eng Sci* 235(10):1891–1908
39. Lay M, Thajudin NLN, Hamid ZAA, Rusli A, Abdullah MK, Shuib RK (2019) Comparison of physical and mechanical properties of PLA, ABS and nylon 6 fabricated using fused deposition modeling and injection molding. *Compos B Eng* 176:107341
40. Kamaal M, Anas M, Rastogi H, Bhardwaj N, Rahaman A (2021) Effect of FDM process parameters on mechanical properties of 3D-printed carbon fibre–PLA composite. *Prog Addit Manuf* 6:63–69
41. Kagawa H, Umezu Y, Sakaue K, Koyanagi J (2023) Numerical simulation for the tensile failure of randomly oriented short fiber reinforced plastics based on a viscoelastic entropy damage criterion. *Composites Part C Open Access* 10:100342
42. Bhandari S, Lopez-Anido RA, Wang L, Gardner DJ (2020) Elastoplastic finite element modeling of short carbon fiber reinforced 3D printed acrylonitrile butadiene styrene composites. *Jom* 72:475–484
43. Muna II, Mieloszyk M (2021) Temperature influence on additive manufactured carbon fiber reinforced polymer composites. *Materials* 14(21):6413
44. Schiavone N, Verney V, Askanian H (2020) Effect of 3D printing temperature profile on polymer materials behavior. *3D Print Addit Manuf* 7(6):311–325
45. Coppola B, Cappetti N, Di Maio L, Scarfato P, Incarnato L (2018) 3D printing of PLA/clay nanocomposites: influence of printing temperature on printed samples properties. *Materials* 11(10):1947
46. Shen Z, Lu L, Sun J, Yang F, Tang Y, Xie Y (2015) Wear patterns and wear mechanisms of cutting tools used during the manufacturing of chopped carbon fiber. *Int J Mach Tools Manuf* 97:1–10
47. Kumar MS, Farooq MU, Ross NS, Yang C-H, Kavimani V, Adediran AA (2023) Achieving effective interlayer bonding of PLA parts during the material extrusion process with enhanced mechanical properties. *Sci Rep* 13(1):6800
48. Mahapatra S, Patnaik A (2009) Study on mechanical and erosion wear behavior of hybrid composites using Taguchi experimental design. *Mater Des* 30(8):2791–2801
49. Tsui K-L (1992) An overview of Taguchi method and newly developed statistical methods for robust design. *IIE Trans* 24(5):44–57
50. Ku J, Rao SS, Chen L (1998) Taguchi-aided search method for design optimization of engineering systems. *Eng Optim* 30(1):1–23
51. Sommacal S, Matschinski A, Drechsler K, Compston P (2021) Characterisation of void and fiber distribution in 3D printed carbon-fiber/PEEK using X-ray computed tomography. *Compos A Appl Sci Manuf* 149:106487
52. Tao Y, Kong F, Li Z, Zhang J, Zhao X, Yin Q, Xing D, Li P (2021) A review on voids of 3D printed parts by fused filament fabrication. *J Market Res* 15:4860–4879
53. Sakai M, Miyajima T, Inagaki M (1991) Fracture toughness and fiber bridging of carbon fiber reinforced carbon composites. *Compos Sci Technol* 40(3):231–250
54. Chrzanowska E, Gierszewska M, Kujawa J, Raszewska-Kaczor A, Kujawski W (2018) Development and characterization of polyamide-supported chitosan nanocomposite membranes for hydrophilic pervaporation. *Polymers* 10(8):868

Publisher's Note Springer Nature remains neutral with regard to jurisdictional claims in published maps and institutional affiliations.

Springer Nature or its licensor (e.g. a society or other partner) holds exclusive rights to this article under a publishing agreement with the author(s) or other rightsholder(s); author self-archiving of the accepted manuscript version of this article is solely governed by the terms of such publishing agreement and applicable law.